Atmos. Chem. Phys., 11, 1355–1366, 2011
www.atmos-chem-phys.net/11/1355/2011/
doi:10.5194/acp-11-1355-2011

Atmospheric Chemistry and Physics

Coincident measurements of PMSE and NLC above ALOMAR (69° N, 16° E) by radar and lidar from 1999–2008

N. Kaifler, G. Baumgarten, J. Fiedler, R. Latteck, F.-J. Lübken, and M. Rapp

Leibniz Institute of Atmospheric Physics at the Rostock University, Kühlungsborn, Germany

Received: 11 August 2010 – Published in Atmos. Chem. Phys. Discuss.: 26 October 2010
Revised: 21 January 2011 – Accepted: 30 January 2011 – Published: 16 February 2011

Abstract. Polar Mesosphere Summer Echoes (PMSE) and Noctilucent Clouds (NLC) have been routinely measured at the ALOMAR research facility in Northern Norway (69° N, 16° E) by lidar and radar, respectively. 2900 h of lidar measurements by the ALOMAR Rayleigh/Mie/Raman lidar were combined with almost 18 000 h of radar measurements by the ALWIN VHF radar, all taken during the years 1999 to 2008, to study simultaneous and common-volume observations of both phenomena. PMSE and NLC are known from both theory and observations to be positively linked. We quantify the occurrences of PMSE and/or NLC and relations in altitude, especially with respect to the lower layer boundaries. The PMSE occurrence rate is with 75.3% considerably higher than the NLC occurrence rate of 19.5%. For overlapping PMSE and NLC observations, we confirm the coincidence of the lower boundaries and find a standard deviation of 1.26 km, hinting at very fast sublimation rates. However, 10.1% of all NLC measurements occur without accompanying PMSE. Comparison of occurrence rates with solar zenith angle reveals that NLC without PMSE mostly occur around midnight indicating that the ice particles were not detected by the radar due to the reduced electron density.

1 Introduction

The low temperatures of the polar summer mesopause region allow for the formation of ice particles, giving rise to phenomena termed polar mesospheric summer echoes (PMSE) and noctilucent clouds (NLC). Although the presence of ice particles is crucial to either, PMSE and NLC differ in the physical mechanisms that create them and require different observation techniques such as radar and lidar. The combination of both allows to gain insight into the processes relevant for the creation of PMSE.

PMSE are strong radar echoes caused by electron density irregularities at the Bragg scale, which is the radar half wavelength for monostatic radars, and are observed at several radar wavelengths. Discovered by Ecklund and Balsley (1981), the mechanism that allows for the maintaining of such structures in this environment was an open question for a long time. Reviews of PMSE observations and theory can be found in Cho and Röttger (1997) and Rapp and Lübken (2004). Following an idea by Kelley et al. (1987) and Cho et al. (1992) the currently most generally accepted theory of PMSE relies on the coupling of electrons to charged aerosols (i.e. ice particles) by ambipolar forces that lead to a reduced electron diffusivity and therefore an enhanced Schmidt number (see Cho et al., 1992; Rapp and Lübken, 2003, for details). The formation of structures at the scale of a few meters in the altitude range of 80–90 km is attributed to turbulent processes (e.g. Lübken et al., 2009) given that a minimum electron number density of 300–500 cm^{-3} is exceeded (Rapp et al., 2002). A dependence on background ionization is also deduced from experiments that showed that PMSE are stronger inside the auroral oval compared to sites inside the polar cap like Resolute Bay where ionization is lower (Swarnalingam et al., 2009).

PMSE is sensitive to ice particles of any size. In favourable conditions, ice particles grow to about 50 nm (Baumgarten and Fiedler, 2008) and eventually become visible as noctilucent clouds, possible to be observed by naked eye in twilight. The first observations of these silvery-white shining clouds date back to 1885 (Backhouse, 1885; Jesse, 1885; Leslie, 1885). The first measurements by lidar succeeded in 1989 (Hansen et al., 1989). Today, NLC are routinely measured by lidar technique (von Cossart et al., 1999) or satellite (Hervig et al., 2009b). With typical number

Correspondence to: N. Kaifler
(n.kaifler@iap-kborn.de)

densities of 100 cm^{-3} (Hervig et al., 2009a) the large particles cause strong backscatter at optical wavelengths. We note that the satellite experiment SOFIE observes ice clouds more often than PMSE is measured by radar (Hervig et al., 2011). Lidar measurements are sensitive to ice particles larger than 10 to 20 nm only (e.g. Baumgarten et al., 2008), leading to smaller occurrence rates, and do not give evidence about smaller ice particles that might still generate PMSE. When speaking of NLC in the following, we refer to lidar measurements of NLC. Consequently, the observation of NLC is directly linked to the presence of ice particles larger than about 15 nm. In a simple picture, ice particles form around the cold mesopause and grow as they sediment by gravitation to lower altitudes where they finally sublimate when entering regions with higher temperature. Li et al. (2010) have recently derived size distributions of ice particle radii from radar measurements consistent with this picture. In this way it can be understood that PMSE occur more frequently than NLC, in a larger altitude range and that NLC are embedded into the lower part of the PMSE layer. However, dynamic processes of the MLT region like turbulence and gravity wave activity strongly influence the growth of ice particles and formation of layers. Since ice particles are very sensitive to temperature, the altitudes and layer width of NLC or PMSE are very suitable to test atmospheric models (e.g. Lübken et al., 2008). The observation of common-volume PMSE and NLC might therefore provide an insight into underlying processes that cannot be derived from observations of PMSE or NLC alone.

Open questions are related to the interplay of parameters of the background atmosphere such as temperature, water vapour and electron density and dynamical processes such as turbulence and gravity waves regarding their role in the formation of PMSE and NLC. Such understanding is crucial to the interpretation of PMSE and NLC measurements. Direct measurements of temperature in this altitude range, for example, are very limited at this latitude, whereas PMSE and NLC can be routinely measured. Quantification of the link between PMSE and NLC, including the observations of NLC without PMSE in the same volume, is suited to test PMSE theories and comparison of the lower boundaries of both phenomena allows to assess sublimation rates and the strength of the coupling of the layers.

Several attempts to investigate NLC and PMSE simultaneously were made using camera observations from ground (Taylor et al., 1989; Kirkwood et al., 1995). The first observation of simultaneous and common-volume observations of NLC measured by lidar and PMSE were published by Nussbaumer et al. (1996), who presented four cases and identified tightly and loosely coupled layers. This dataset, obtained at ALOMAR, was extended by von Zahn and Bremer (1999) presenting 22 cases and defining three types of layers, namely PMSE and NLC in a common volume, which accounted for 63% of all cases, layers with temporal differences (16%) and spatial differences (21%). PMSE and NLC have also been observed at other locations, among them Spitsbergen (Lübken and Höffner, 2004; Lübken et al., 2004), Poker Flat, Alaska (Taylor et al., 2009) and Antarctica (Klekociuk et al., 2008). In all observations, a striking coincidence of lower boundaries of both PMSE and NLC layers were observed at times, but not always.

In this paper, we analyze a large dataset during nine NLC seasons of combined lidar and radar observations. These measurements cover all local times due to full daylight capability of the ALOMAR RMR-lidar. This dataset allows us to derive statistics beyond case studies of single events. We define several cases based on occurrence and relative layer altitudes, calculate occurrence rates of joint and sole PMSE/NLC observations, in total as well as as function of year, local time and solar zenith angle, and quantify the previously observed coincidences of lower boundaries.

2 Instruments and data processing

We use data from the ALWIN radar and ALOMAR Rayleigh/Mie/Raman lidar that are located on the North Norwegian island of Andøya (69.3° N, 16.0° E). Both instruments are separated by less than 3 km, such that a zenith-looking lidar beam samples inside the radar volume.

2.1 Radar

The ALWIN VHF radar operates at 53.5 MHz and has a half-power beam width of 6.5°, resulting in a radar volume with a diameter of ≈10 km at 83 km altitude. Technical information is given by Latteck et al. (1999). We analyze the relative signal power of backscattered echo power P (in dB) at a 300 m vertical and 5 min temporal resolution. Background noise of cosmic origin was subtracted from the signal. Additionally, typical contaminations of radar measurements like interfering signals were removed from the dataset. PMSE are detected from 5-min mean values of the relative signal power. A PMSE event is defined as a power enhancement above the a detection threshold but for a minimum duration of 20 min (i.e., 4 consecutive 5-min averages) in one height channel. This excludes single events like e.g. meteor echoes but does not affect the PMSE occurrence rate. Due to a technical problem during the year 2003 that affected the estimation of PMSE bottom altitudes we neglect this years data when comparing bottom altitudes. The characteristics of the radar system and configuration of the experiment determine a threshold for the detection of significant echoes like PMSE. We detect PMSE by attributing every time-altitude bin that exceeds a threshold of $P_{\mathrm{thr}} = 5$ dB to a PMSE layer. By this, the layer edge is defined by the 5 dB-isoline. An overview of PMSE measurements with this instrument was recently published by Bremer et al. (2009).

2.2 Lidar

The ALOMAR Rayleigh-/Mie-/Raman (RMR) lidar employs two lasers and two tiltable telescopes of 1.8 m diameter to measure the volume backscatter coefficient β (in units of $10^{-10}\,\mathrm{m^{-1}\,sr^{-1}}$) at 532 nm. The horizontal distance to zenith varies between 0 and 30 km at NLC altitudes, according to different tilting angles. When lidar measurements with both systems were conducted, we use only data from the north-west-telescope. A description of the instrument is given by von Zahn et al. (2000) and the principle of the data retrieval for NLC analysis is described by Fiedler et al. (2009). The range and time resolution of the lidar changed over the years from 150 m and 3 min to 50 m and 1 min since 2007. The data was smoothed by a binomial filter with 475 m FWHM. To yield a uniform dataset the data was re-sampled to 40 m vertical and 1 min temporal resolution using bi-cubic splines. We enhanced the signal-to-noise ratio for detection of NLC signatures by first analyzing the data with a 4 to 6 min temporal average and a 30% neighbour filter in a 25 min and 1.5 km environment. This filter suppresses lonesome noise (or NLC) events which are not surrounded by other significant NLC signatures in the given time-altitude environment. Here we test the significance by requiring that $\beta > \Delta\beta$, with $\Delta\beta$ being the 1σ measurement uncertainty. $\Delta\beta$ depends on local time and improved over the years, but is typically below $1\times10^{-10}\,\mathrm{m^{-1}\,sr^{-1}}$. The resulting NLC signatures were then re-binned to a fixed 1 min grid. The lidar sounding volume is about $10\,\mathrm{m}\times10\,\mathrm{km}\times500\,\mathrm{m}$, given typical horizontal wind speeds at NLC altitude of $\approx30\,\mathrm{m\,s^{-1}}$ as measured by the MF and meteor radars at ALOMAR (e.g. Singer et al., 2005). For our analysis, we accept a NLC signature if the peak brightness exceeds a threshold of $\beta_{\mathrm{thr}} = 4\times10^{-10}\,\mathrm{m^{-1}\,sr^{-1}}$, which is the long-year detection limit of the lidar as discussed by Fiedler et al. (2009), who also published an overview of NLC measurements with this instrument.

2.3 Combination of formatted instrument data

Both PMSE and NLC measurements are converted to a common data format, which are daily, midnight-centered time-altitude matrices. PMSE and NLC signals were determined as explained above, with the PMSE power limited to $P > 5$ dB and NLC profiles selected by a peak backscatter exceeding $4\times10^{-10}\,\mathrm{m^{-1}\,sr^{-1}}$. Similar to the pre-processing of the lidar data, we apply the following algorithm to these NLC or PMSE matrices: to discriminate for single false detections in isolated bins (sometimes termed spikes or needles), which is especially important for PMSE data, every bin with PMSE or NLC that is not neighboured by at least two other non-zero bins in a neighbourhood of 8 is removed. Additionally, every bin that is not neighboured by at least one bin in the two bins before and after at the same altitude is also removed, which is to eliminate isolated profiles. Such a neighbour filter was applied to improve the data quality by removing events that only occur in one time-altitude-bin. As both NLC and PMSE typically occur in layers wider than our altitude resolution, this does not effect these layers but removes single bins that are presumably noise or of other origin. In radar data, meteor echoes occur in single events and are successfully eliminated by this method, which is commonly used (Latteck et al., 2007). The total amount of data removed by this method is negligible and the overall occurrence rate of PMSE or NLC is not effected, as these are calculated per time bin. However, this procedure, together with the careful choice of the thresholds ensures the robustness of our altitude retrieval method by removing isolated detections while keeping the well-defined cloud layers intact. To account for comparability of the two datasets, NLC data is then smoothed in time with a gliding average of 5 min to match the temporal resolution of the radar data. The top and bottom altitudes of PMSE or NLC layers are retrieved by finding the lowest or highest altitude with PMSE or NLC signal in each profile. PMSE and NLC datasets are then combined by matching times. The resulting temporal resolution is 5 min.

3 Analysis of combined dataset

We analyze data of nine summer seasons from 1999 to 2008, each lasting from 1 June to 15 August, which is the season for NLC at this location. The ALWIN radar was in operation during 17 898 h, detecting PMSE by the above mentioned method in 13 900 h, resulting in an overall occurrence rate of 77.6 ± 0.1%. The RMR lidar, with its operation being restricted to good weather conditions, took data in 2890 h. NLC were observed in 565 h, which yields a NLC occurrence rate of 19.5 ± 0.2%. A significant amount of this data was obtained with zenith-looking lidar beams (1931 h). The lidar measurements are almost completely included in the combined dataset of radar and lidar, which comprises 2788 h of data when both instruments were in operation (termed "simultaneous measurements"). Figure 1 shows the dataset regarding year, local time and solar zenith angle. The data is well-distributed over the years and in local time. However, care must be taken interpreting extreme solar zenith angles, as solar zenith angles below 50° are only achieved prior to 27 July and angles above 90° only from 21 July at this location. In between however, solar zenith angles are well distributed throughout the season.

We have selected six examples of joint observations of PMSE and NLC extending over several hours that demonstrate some common features (Fig. 2). All times displayed are Local Time (LT), which corresponds to UT+1 h and is close to Local Solar Time at the location of ALOMAR (Fiedler et al., 2005). NLC is typically located in the lower part of the PMSE layer (Fig. 2a and f), but may also, at times, exist without PMSE in the common volume (Fig. 2a and b). A striking example of exactly coinciding layers, not only in altitude, but also in width, is observed on 7 July 2007

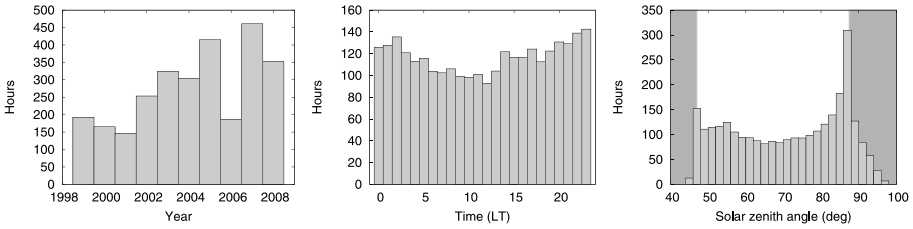

Fig. 1. Simultaneous measurement times of the ALWIN radar and RMR lidar in hours as a function of year, local time and solar zenith angle. Extreme solar zenith angle (shaded) are not discussed because they are not distributed equally throughout the season.

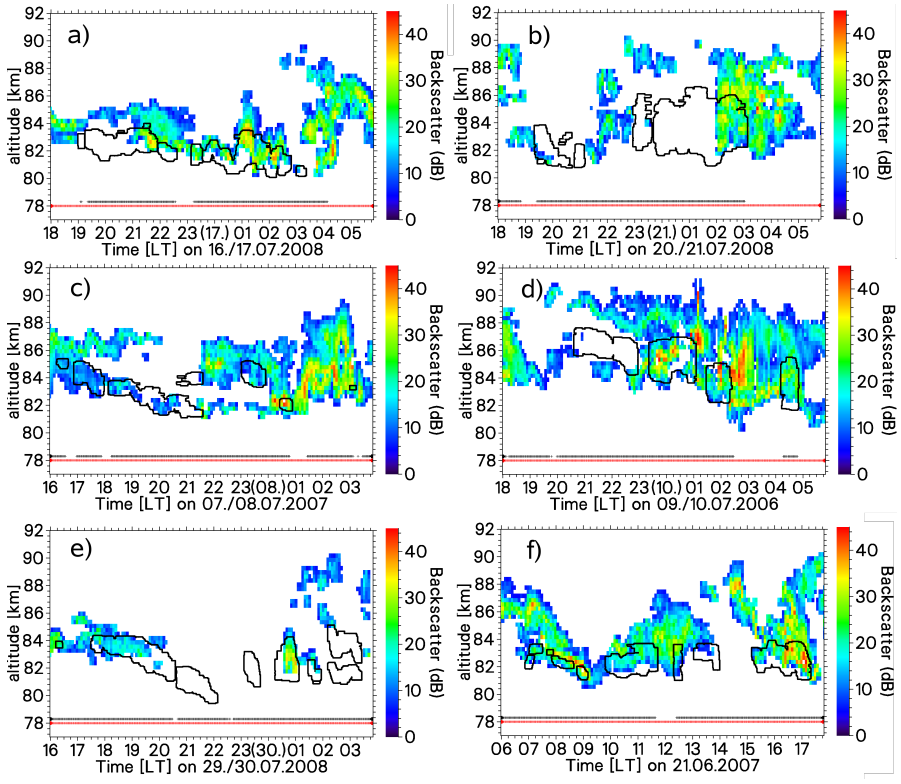

Fig. 2. Examples of joint PMSE (color, limited to >5 dB) and NLC (contour, limited to $\beta > \Delta\beta$) observations. Measurement times are indicated by red crosses for radar and in black crosses for lidar.

from 17:00 to 22:00 LT (Fig. 2c). But NLC layers may also be well embedded in the PMSE layer (Fig. 2d) or continue to sediment further down when PMSE has already vanished (Fig. 2e). As these few examples already show, both PMSE and NLC layers are highly variable (existence over large altitude range, varying power and layer width, sudden onsets) and susceptible to wave activity with typical periods of approximately one hour (Fig. 2a, c, d) even including effects of multiple layering (Fig. 2d, e). In the following, an attempt shall be made to characterize common features by defining cases and quantifying their occurrence.

3.1 Characterization in terms of occurrence and altitude relation

3.1.1 Definition of cases

We divide the simultaneous measurements into five cases, sketched in Fig. 3, depending on the occurrence of PMSE or NLC sorted by approximate commonness: I. PMSE without NLC, II. neither PMSE nor NLC, III. PMSE above NLC, IV. PMSE and NLC overlapping, V. PMSE below NLC and VI. NLC without PMSE. Case IV is further divided according to the altitude relation of the overlapping layers: (a) PMSE above and inside NLC, (b) PMSE above, inside and below NLC, (c) PMSE inside NLC and (d) PMSE inside and below

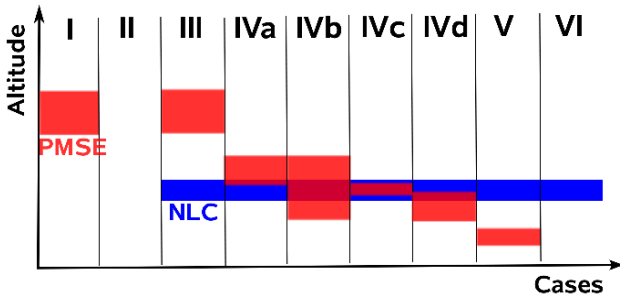

Fig. 3. Schematic drawing of cases of PMSE and NLC occurrence. They are distinguished by the occurrence and relative top and bottom altitudes.

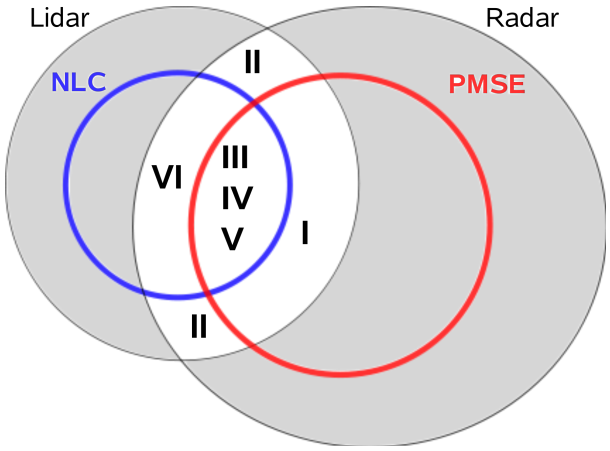

Fig. 4. Schematic drawing of lidar and radar data set (big circles). The colored circles include the measurements where NLC or PMSE were detected. The regions I to VI make up the simultaneous measurements according to the PMSE and/or NLC occurrence. The shaded areas are discarded. Areas are not to scale.

NLC. The number of hours for each case in our dataset is listed in Table 1. PMSE without NLC is the most likely case (I), which is to be expected regarding a generally high PMSE occurrence rate and comparably low NLC occurrence rate. When NLC occurs, PMSE occurrence is also very likely (III to V). "NLC without PMSE" is seldom compared to total measurement hours, but not negligible (VI). NLC is mostly embedded, or at least overlapped, with a PMSE layer (IVb, IV). Case IVc, IVd and V are not considered further because of low statistics.

3.1.2 PMSE/NLC occurrence rates

These absolute numbers (in measurement hours) of the cases defined in Sect. 3.1.1 are now combined and related to each other in order to assess relative occurrence rates of joint or sole observations of PMSE and/or NLC. Among the possible relations we select the following:

Table 1. Statistics of PMSE and NLC measured by the ALWIN radar and ALOMAR RMR lidar in the years 1999–2008. The combined dataset ("simultaneous measurements") is split into cases I to VI regarding the occurrence of PMSE and/or NLC. Overlapping layers (case IV) are further split regarding their altitude relation.

Measurements lidar | radar	2890 h	17898 h
Measurements NLC | PMSE	565 h	13900 h
Simultaneous measurements (I to VI)	2788 h	100%
Simultaneous observations of PMSE and NLC (III+IV+V)	489 h	
I (PMSE without NLC)	1620 h	58.1%
II (neither PMSE nor NLC)	626 h	22.4%
III (PMSE above NLC)	47 h	1.6%
IV (PMSE and NLC overlapping)	438 h	15.7%
IVa (PMSE above and inside NLC)	204 h	
IVb (PMSE above, inside and below)	213 h	
IVc (PMSE inside NLC)	16 h	
IVd (PMSE inside and below NLC)	5 h	
V (PMSE below NLC)	4 h	0.1%
VI (NLC without PMSE)	53 h	1.9%

1. P(PMSE): probability of observing PMSE relative to all times,
2. P(NLC): probability of observing NLC relative to all times,
3. P(PMSE|NLC) ("PMSE given NLC"): probability of observing PMSE during NLC measurements,
4. P(NLC|PMSE) ("NLC given PMSE"): probability of observing NLC during PMSE measurements,
5. $P(\text{NLC}|\overline{\text{PMSE}})$ ("NLC without PMSE"): probability of observing NLC during the absence of PMSE.

The corresponding equations and resulting numbers are given in Table 2 and Fig. 4 visualizes the datasets as a set diagram. It has long been known that PMSE and NLC are not independent phenomena, first of all from both their occurrence during the summer season in the mesopause region and many other observations that led to our current understanding. In the here defined probabilities, this dependence is reflected by $P(\text{PMSE}|\text{NLC}) > P(\text{PMSE})$ as well as $P(\text{NLC}|\text{PMSE}) > P(\text{NLC})$, which means that the occurrence of one is enhanced if the other is present, or simply that they are positively linked. Stochastic independence on the other hand would require that the occurrence rates do not change if a random subset of the dataset is selected. In practice this means that when we know the radar observes PMSE when starting the lidar, we can expect to see NLC with a 20% increased probability compared to the average value. The same is true the other way around. On the other hand, if the radar reports missing PMSE, our chance of observing NLC sinks from the independent occurrence rate of 19.5% to only 7.8%. Of all NLC observed, 89.9% are accompanied by PMSE,

Table 2. Probabilities of PMSE and NLC occurrence for different selection criteria. Statistical errors were calculated as in Fiedler et al. (2009). Figure 4 visualizes the sets used in these equations. Note that the total and conditional probabilities are connected by the law of total probability, which is, in our notation, $P(\text{PMSE}) = P(\text{PMSE}|\text{NLC}) \cdot P(\text{NLC}) + P(\text{PMSE}|\overline{\text{NLC}}) \cdot P(\overline{\text{NLC}})$ with $P(\overline{\text{NLC}}) = 100\,\% - P(\text{NLC})$.

(1)	$P(\text{PMSE}) = \frac{\text{I+III+IV+V}}{\text{I+II+III+IV+V+VI}}$	75.3±0.2%
(2)	$P(\text{NLC}) = \frac{\text{III+IV+V+VI}}{\text{I+II+III+IV+V+VI}}$	19.5±0.2%
(3)	$P(\text{PMSE}\|\text{NLC}) = \frac{\text{III+IV+V}}{\text{III+IV+V+VI}}$	89.9±0.4%
(4)	$P(\text{NLC}\|\text{PMSE}) = \frac{\text{III+IV+V}}{\text{I+III+IV+V}}$	23.2±0.3%
(5)	$P(\text{NLC}\|\overline{\text{PMSE}}) = \frac{\text{VI}}{\text{II+VI}}$	7.8±0.3%

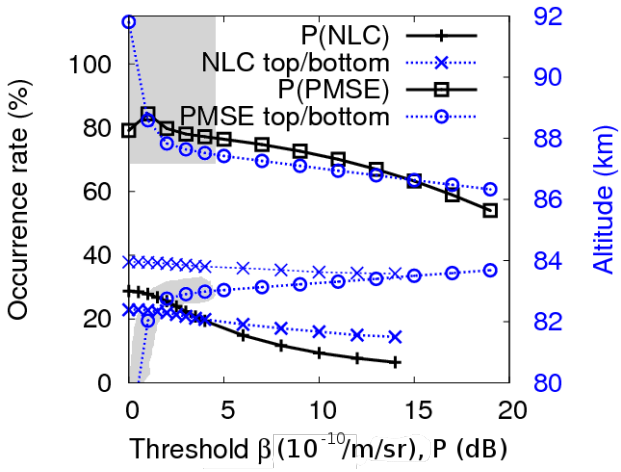

Fig. 5. Dependence of PMSE and NLC occurrence rates (black, left axis) and averaged top and bottom altitudes of PMSE and NLC (blue, right axis) on the threshold P_{thr} or β_{thr}.

leaving 10.1% of all NLC measurements to occur without PMSE.

3.2 Robustness of method

To demonstrate the robustness of our method, we address the aspects of representative sampling, common-volume measurements and the influence of the choice of the threshold in this section.

The radar dataset was considerably reduced (to 15.6% of the total data) to match the less frequent lidar measurements. Mean PMSE occurrence rates derived from the complete (77.6%) and the reduced dataset (75.3%) agree nevertheless with respect to natural year-to-year variability, confirming that the reduced sample is representative. Another indication for possible unequal sampling is the yearly mean solar zenith angle that has a standard deviation of 1.9°. Influences of sampling on yearly mean NLC properties however were carefully investigated by Fiedler et al. (2009) and found to be negligible.

A tilted lidar beam of 20° is actually outside the radar volume. However, during 5 min of integration time the ice particles are transported about this range given typical wind speeds as measured by radar. Therefore, tilted lidar measurements might still be considered "common-volume" with a zenith-looking, wide radar beam. We have checked the subset of zenith lidar measurements only and found that the derived numbers for the probabilities (1)–(5) agree within errors, confirming the presumption of a common volume. Therefore, the data from tilted beams is included in our analysis.

The chosen of the detection threshold, essentially selecting PMSE and NLC events regarding their power or brightness, influences both occurrence rates and altitudes. The more events can be taken into account, the higher is the occurrence rate (Fig. 5). In case of the radar dataset, the threshold however can only be lowered to the noise limit of 5 dB. At lower thresholds, random noise prevents a robust estimation of the PMSE layer. Figure 2 of Bremer et al. (2003) is based on signal-to-noise ratio rather than relative signal power but otherwise shows the same results considering our different noise suppression algorithm described in Sect. 2.3. For the lidar dataset, already including significant NLC profiles only, a limit of about $\beta_{\text{thr}} = 2 \times 10^{-10}\,\text{m}^{-1}\,\text{sr}^{-1}$ marks the sensitivity of the instrument. Figure 5 also shows the effect on altitudes. PMSE layers are thinned using higher thresholds because the layer is restricted to its bright core. For NLC, as bright NLC layers tend to be at lower altitudes, a high threshold which includes only bright NLC also yields layers at slightly lower altitudes. We note that despite the many observations of coinciding lower boundaries, in average of all PMSE and NLC detected, the PMSE lower boundary is located several hundred meters above the NLC lower boundary and this separation does not vanish for any combination of valid thresholds. Although a noise-free radar system might detect wider PMSE layers, we do not believe this is a sensitivity issue considering our results of the next section which confirm a striking coincidence of lower boundaries in the case of simultaneous observations of PMSE and NLC. The explanation is rather, that the average PMSE is determined by ice particles of different properties (e.g. smaller radius) than the particles the average NLC is made of.

Having introduced and demonstrated the suitability of our analysis method, we turn to a closer inspection of the relations of PMSE and NLC bottom altitudes in our large dataset and secondly quantify the occurrence of NLC without PMSE, a phenomenon that demonstrates that the presence of ice particles is only a necessary but not a sufficient condition for PMSE.

Table 3. Mean layer boundaries, separation of NLC and PMSE bottom altitudes and NLC brightness for each of the defined cases. Additionally, electron density from the IRI model is given. Data of the years 1999–2008 is averaged.

	PMSE			NLC			β (10^{-10} m^{-1} sr^{-1})	NLC−PMSE	el. dens.
Case	z_{bot} (km)	z_{top} (km)	Δz (km)	z_{bot} (km)	z_{top} (km)	Δz (km)	mean, median	Δz_{bot} (km)	n_e (cm^{-3})
I to VI	82.99±0.01	87.39±0.01	4.40±0.01	82.11±0.02	83.79±0.02	1.68±0.03	9.8±0.1, 7.27	−0.88	575±1
III+IV+V	82.10±0.02	87.13±0.03	5.03±0.04	82.12±0.02	83.81±0.02	1.69±0.03	9.8±0.1, 7.31	0.02	534±2
I	83.27±0.02	87.47±0.02	4.20±0.03						604±2
II									538±2
III	85.36±0.09	87.18±0.08	1.82±0.12	81.92±0.05	83.39±0.06	1.47±0.08	9.4±0.3, 7.30	−3.44	490±4
IV	81.74±0.02	87.14±0.03	5.40±0.04	82.08±0.02	83.80±0.02	1.72±0.03	9.9±0.1, 7.35	0.34	536±2
IVa	82.25±0.02	86.71±0.05	4.46±0.05	81.71±0.02	83.54±0.03	1.83±0.04	11.5±0.2, 8.80	−0.54	520±3
IVb	81.22±0.03	87.90±0.04	6.68±0.05	82.49±0.02	83.96±0.03	1.47±0.04	8.3±0.1, 6.07	1.27	554±4
VI				81.87±0.08	83.57±0.08	1.70±0.11	10.2±0.4, 6.98		484±4

4 PMSE/NLC bottom altitudes in common-volume observations

The coincidence of PMSE and NLC bottom altitudes was reported from different locations, first by von Zahn and Bremer (1999) at Andøya, later on by Lübken and Höffner (2004) in Spitsbergen, Klekociuk et al. (2008) in Antarctica and others. Having in mind that PMSE is sensitive to a wider spectrum of ice particle sizes, such a missing separation hints at a very rapid sublimation. Typical temperature gradients at NLC altitude during the NLC season are $-4.4\,\mathrm{K\,km^{-1}}$ (after Lübken, 1999) and models predict coincidences within ≈200 m (see also Lübken et al., 2004). A sedimentation velocity of NLC particles of $\approx 1\,\mathrm{km\,h^{-1}}$ restricts the lifetime of particles fallen below the lidar detection threshold to several minutes until they can no longer sustain PMSE. In consequence, a small or zero separation between lower boundaries of PMSE and NLC implies that the lidar measurements of the NLC lower boundary represent the lower boundary of the ice layer well.

To determine such small or even zero separations between measurements obtained by two very different instruments observing two different phenomena remains challenging. In our dataset, the vertical resolution is 300 m for the radar and 40 m, resp. 150 m, for the lidar, being smoothed with a gliding average of 475 m. The horizontal resolution of lidar and radar is however different by three orders of magnitude with the width of the radar beam of ≈10 km and that of the lidar beam of ≈10 m. Additionally, small-scale structures in ice layers as known from visual NLC observations and ice layer tilts as known from twin lidar measurements of NLC contribute to the uncertainty. Keeping this in mind, we estimate the possibly best resolution of altitude differences to be on the order of 500 m. This is a good resolution knowing the natural variability of the bottom altitudes during one day is 2 km for PMSE and 1.2 km for NLC, such that a coincidence within 500 m already indicates a strong coupling of the layers. Nevertheless a large dataset from which average values with low statistical error can be obtained, is of advantage. We therefore study the altitude relations of the layers for the different cases we have defined first, and then turn to the quantification of the bottom altitude coincidence in simultaneous and common-volume observations of PMSE and NLC by comparing single measurements.

Table 3 lists both top and bottom altitudes of the PMSE and NLC layers and the average NLC peak brightness for the defined cases. In average of all measurements (case I to VI), no matter if NLC were present or not, the mean layer width of PMSE is 4.4 km. The bottom of the PMSE layer is then located ≈900 m above the NLC lower boundary, as was already indicated in Sect. 3.2. In case of NLC (no matter if PMSE were present or not) the layer width is 1.7 km. As PMSE are sensitive to ice particles of all sizes, this means that in average PMSE conditions, ice particles are hardly large enough to be visible as NLC by the lidar and the average PMSE altitude, connected to the largest number density of ice particles, lies above typical NLC altitudes. Only in conditions cold enough providing ample time for ice particles to grow as they sediment, PMSE occurrence extends to lower altitudes, increasing its layer width. In this case (our case IV), the bottom altitude of PMSE is even found 340 m below the NLC lower boundary. This complies with the understanding that sublimating particles, having become invisible, continue to cause PMSE for a short time until they are sublimated completely. The here mentioned numbers are significant, as they are obtained by averaging over a large number of measurements. The statistical errors are also given in Table 3. In the typical case where NLC is embedded in the lower part of the PMSE layer (case IVb), the PMSE layer is 6.7 km wide. However, our brightest NLC observations are accompanied by PMSE that, although shifted to lower altitudes, do not reach below the NLC lower altitude (case IVa). It seems that in the presence of such large ice particles, or bright NLC, NLC can reach further down than PMSE. Although it is possible that very weak PMSE below the detection threshold of the radar exist, case IVb proves that the detection of low-altitude PMSE is possible and is not restricted by sensitivity of the instrument. This indicates that ice particles are only

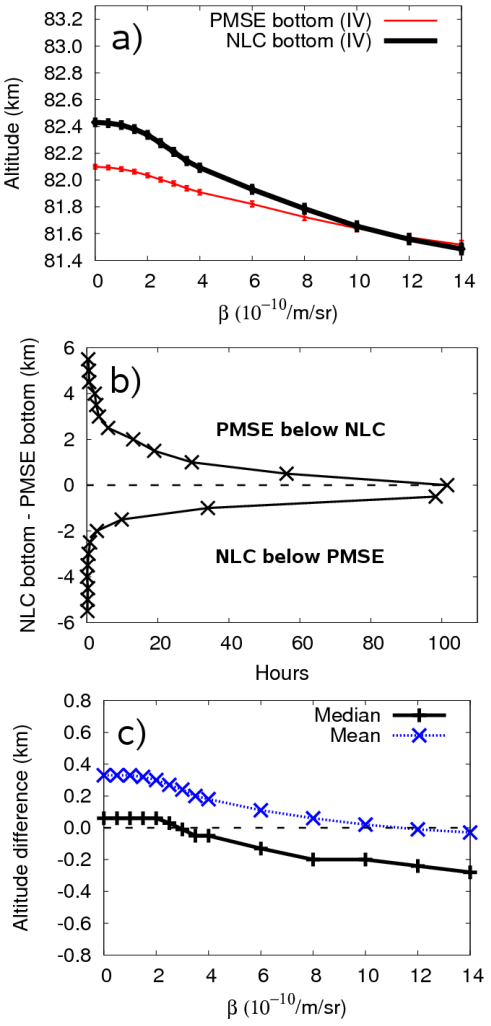

Fig. 6. **(a)** Average bottom altitudes of PMSE and NLC in case of simultaneous observations of NLC and PMSE (case IV) as a function of the threshold β_{thr}. **(b)** Distribution of separation of PMSE and NLC bottom altitudes for β_{thr}=4×10^{-10} m^{-1} sr^{-1} of combined observations. **(c)** Mean and median of the distribution in **(b)** as a function of β_{thr}.

a necessary but not a sufficient condition for PMSE formation. Other necessary conditions are ionization and turbulent activity, which might be limited especially at low altitudes. This restriction would then also explain our observations of PMSE located way above NLC layers (case III). Since it is known that PMSE can develop stable double layer structures (Hoffmann et al., 2005, 2008), this observation arises when a lower layer of such a double layer structure, that would have coincided with the NLC layer, has faded out and only the upper layer remains.

To take the study of the dependence of PMSE altitudes on NLC brightness on, we select NLC events regarding their brightness by choice of the threshold. As mentioned

Table 4. Distribution of difference of lower boundaries of PMSE and NLC (Δz_{bot}=$z_{\mathrm{bot,NLC}}$−$z_{\mathrm{bot,PMSE}}$), 1999–2008. β_{thr} is given in 10^{-10} m^{-1} sr^{-1}.

	β_{thr}=4	β_{thr}=4 zenith only	β_{thr}=0
Hours	386	240	560
Median (km)	−0.05	−0.05	0.06
Mean (km)	0.18	0.24	0.33
Std.dev. (km)	1.26	1.35	1.29
Skewness	2.05	1.74	1.80
$\lvert\Delta z\rvert$<250 m (%)	27.4±0.7	26.3±0.8	26.8±0.5

before (see Fig. 5 and discussion) a higher NLC threshold removes dim NLC from the sample set, and as those are usually located at higher altitudes (anti-correlation of altitude and brightness, e.g. Chu et al., 2006), the NLC bottom altitude decreases with increasing brightness. Figure 6a shows how this correlation also effects accompanying PMSE. The PMSE lower boundary decreases with increasing NLC brightness in a way that it is located below the NLC bottom altitude. However, as NLC become brighter, this separation diminishes. This is consistent with the discussion of case IVa in the previous paragraph and although the amount of data decreases from 560 h at $\beta_{\mathrm{thr}} = 0$ to 130 h at $\beta_{\mathrm{thr}} = 14 \times 10^{-10}$ m^{-1} sr^{-1}, the error of the mean is small (almost within symbol size). We can conclude that the lower boundary of PMSE that accompany NLC (case IV) is below the NLC lower boundary and that in the presence of bright NLC, PMSE reach to lower altitudes, but the lower boundaries are found closer together.

We finally compare the bottom altitudes of simultaneous observations of PMSE and NLC directly to each other. The distribution of differences of bottom altitudes is shown in Fig. 6b. As expected from previous publications on the striking coincidence of lower boundaries, it is centered clearly around zero altitude difference. Statistical properties are listed in Table 4. Both mean and median are not significantly different from zero regarding a resolution of 500 m. In fact, in about 27% of all measurements the bottom altitudes agree within $|\Delta z| < 250$ m, and the standard deviation is 1.26 km, which is comparable to natural variability in one day. These results are in agreement with Lübken et al. (2004), who presented histograms of three events with an estimated standard deviation of 1.6 km and a mean of 300–500 m. Also, our distribution is asymmetric preferring NLC embedded into the PMSE layer, as expected. To rule out any influences of spatial separations due to tilted lidar beams, we restrict the dataset to zenith lidar measurements (Table 4, middle column), but do not obtain significantly changed results. Inclusion of all detectable NLC ($\beta_{\mathrm{thr}} = 0$) also does not improve the coincidence of lower boundaries

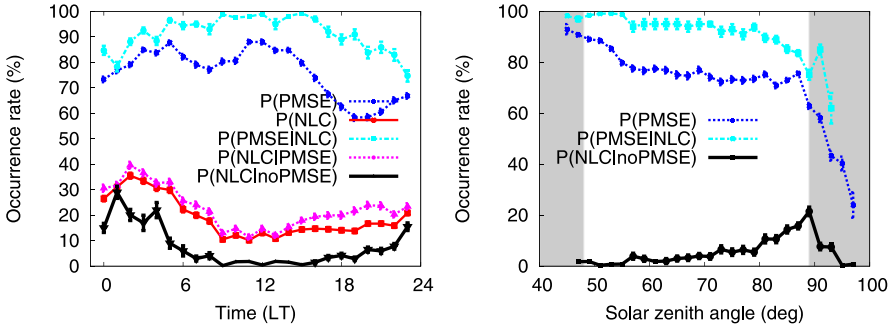

Fig. 7. Occurrence rates as function of local time and solar zenith angle.

further, meaning this result is not limited by the detection threshold chosen here. Selecting NLC by brightness as before, Fig. 6c shows the mean and median of the distribution for $0 < \beta_{\mathrm{thr}} < 14 \times 10^{-10}\,\mathrm{m}^{-1}\,\mathrm{sr}^{-1}$. Both values are close to zero and decrease with increasing threshold, meaning the distribution is slightly shifted to prefer NLC below PMSE as only bright NLC are taken into account, all consistent with our previous analysis.

5 PMSE/NLC occurrence rates and NLC without PMSE

We have mentioned missing ionization or low turbulent activity as possible explanations for the observations of NLC without PMSE. Turbulent activity in this altitude range and especially with respect to variations in altitude or time is difficult to assess and there is limited observational data. Ionization is mainly influenced by Ly-α radiation as described by the Chapman production function and varies $\propto\sqrt{\sec\chi}$ with the solar zenith angle. As derived by Rapp et al. (2008, Appendix A), the radar volume reflectivity depends quadratically on the electron number density n_{e}, using an expression for the refractive index by Hocking (1985). Besides these two mechanisms acting upon PMSE, both PMSE and NLC are subject to thermal tides and therefore exhibit diurnal and semi-diurnal variations. In this section, we will first show the probabilities 1.–5.) from Table 2 as a function of local time and then study these occurrence rates as a function of solar zenith angle, including a comparison with electron number density as derived from a model.

5.1 Variation with local time and solar zenith angle

Figure 7 (left) shows the occurrence rates defined in Table 2 as a function of local time. The PMSE occurrence rate is maximum at 06:00 and 13:00 LT, whereas the NLC occurrence rate has a main maxima at 03:00 LT and only a weak variation owing to the semi-diurnal tide. (Detailed tidal analysis of the data used here are found in Hoffmann et al., 1999 and Fiedler et al., 2005.) The phase shift of three hours between the main maxima of PMSE and NLC may be due to the sensitivity to different-sized ice particle populations that react with different time lags to the background atmosphere. The pronounced maximum of PMSE around noon, however, has previously been attributed to increased electron density due to a maximum in Ly-α induced D-region ionization (Klostermeyer, 1999). During the day (about 09:00 to 19:00 LT), given observations of NLC, the probability to observe PMSE rises significantly to almost 100% (prob. 3.). Accordingly, the probability of observing NLC in the absence of PMSE (prob. 5.) is close to zero. The situation is different in the late evening hours, when PMSE occurrence is at minimum. The probability to observe NLC is enhanced if PMSE is present (prob. 4.), but also the probability to observe NLC without PMSE is enhanced (prob. 5.). It is largest in the early morning hours, with a maximum at 02:00 LT, when NLC occurrence is high.

Figure 7 (right) shows all probabilities as a function of solar zenith angle. As mentioned before, we restrict discussion to solar zenith angles between 48° and 89° as only those are equally distributed within the season. The decreasing electron density with increasing solar zenith angle leads to a slightly declining PMSE occurrence rate. The probability of PMSE measured during NLC displays also decreases with solar zenith angle (prob. 3.). Accordingly, the probability of observing NLC during the absence of PMSE (prob. 5.) is maximum at high solar zenith angles. The probability for NLC without PMSE now seems to be anti-correlated to the PMSE occurrence rate, indicating that a large fraction of these cases are due to reduced electron density.

5.2 Dependence on electron density and correlations

We calculate electron number densities from the International Reference Ionosphere (Bilitza, 1998) at an altitude of 83 km and geographic coordinates 69° N, 16° E. IRI combines various data sources like ionosondes, incoherent scatter radars and instruments on satellite and rockets to derive parameters of the ionosphere. Over the altitude range where PMSE occurs, electron density can vary up to an order of

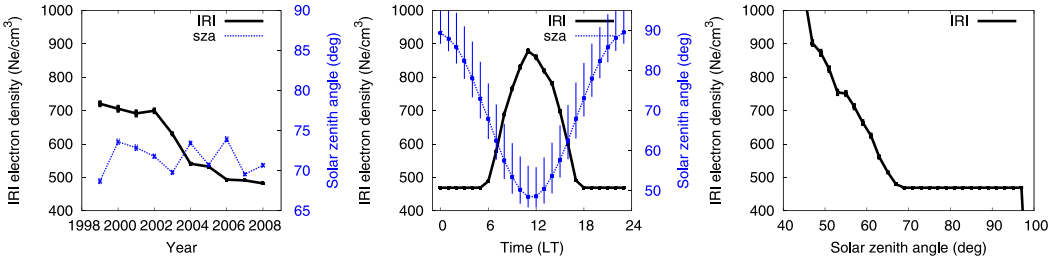

Fig. 8. Electron density (IRI, left axis) and solar zenith angle (right axis) for the time of measurements as a function of year, local time and solar zenith angle. With respect to local time, the seasonal variation of the solar zenith angle is indicated by the bars.

Table 5. Correlation coefficients between PMSE/NLC occurrence rates per local time (12 values, top) and between solar zenith angle and IRI electron density per solar zenith angle (24 values, bottom). In brackets the 95%-confidence interval is given (after David, 1938). The correlation is significant (printed bold), if zero is not included in the confidence interval.

r (LT)	P(PMSE)	P(NLC)	P(NLC|$\overline{\text{PMSE}}$)
P(NLC)	0.19 (−0.20, 0.53)	–	
P(NLC|$\overline{\text{PMSE}}$)	0.00 (−0.38, 0.38)	**0.85 (0.65, 0.96)**	–
r (sza)	P(PMSE)	P(NLC)	P(NLC|$\overline{\text{PMSE}}$)
sza	**−0.90 (−0.60, −0.98)**		
iri	**0.94 (0.52, 0.99)**		**−0.65 (−0.02, −0.88)**
P(PMSE)	–		**−0.74 (−0.91, −0.20)**

magnitude in altitude. However, as we focus on the joint occurrence with NLC that are observed at an altitude of approximately 83 km, we study electron densities at this fixed altitude only. Mean values of electron density as a function of year, time and solar zenith angle are presented in Fig. 8 together with the solar zenith angle. All values were calculated for the actual measurement times and averaged. The yearly mean electron densities are strongly influenced by solar cycle, being maximum in year 1999/2002 and minimum in year 2008 (Fig. 8a). During daytime, electron density is anti-correlated to solar zenith angle and during night, the model assumes it to be at constant level (Fig. 8b), averaging over energetic particle precipitation events that occur at night.

Results of a correlation analysis of the PMSE and NLC occurrence rates, electron densities and solar zenith angles discussed here are listed in Table 5. As a function of local time, the PMSE occurrence rate is neither significantly correlated with the NLC occurrence rate nor with the probability to observe NLC in the absence of PMSE, due to the mixture of thermal tides and influence of electron density. As a function of solar zenith angle however, influence of electron density becomes apparent. Both the PMSE occurrence rate is significantly correlated with electron density and the probability to observe NLC without PMSE is significantly anti-correlated to the PMSE occurrence rate. We take this as indication that observations of NLC without PMSE are due to missing electron density that reduces PMSE in general. Depletion of PMSE connected to low electron density was also observed by Rapp et al. (2009, their Fig. 4) during a rocket flight.

Further strong evidence for the impact of electron density on the occurrence of NLC without PMSE is the mean electron density calculated for all our defined cases as listed in the last column of Table 3. Despite variations with solar cycle on the order of 200 cm^{-3} and day-night-variations of ≈400 cm^{-3}, the mean electron density per case varies as much as 120 cm^{-3}. Significantly lower electron density than average is found for cases VI and III, which is NLC without PMSE at all or with NLC well below PMSE. The largest values for electron density are found for case I, which is PMSE without NLC, further corroborating the dependence on electron density.

6 Conclusions

We have analyzed nine years of PMSE and NLC measurements in the same volume by combining the datasets of the ALWIN radar and ALOMAR RMR lidar at Andøya, Northern Norway. We observe an enhanced occurrence rate of PMSE or NLC if the other phenomena was present, confirming that their occurrence is positively linked. In case of

NLC presence, PMSE is located 880 m lower than its average altitude. For overlapping PMSE and NLC observations, we confirm the coincidence of lower boundaries. 27% of all cases agree within $|\Delta z| < 250$ m, the median of the distribution being -50 m and the standard deviation 1.26 km. More loosely coupled layers might be attributed to turbulent activity or small-scale gravity waves leading to fast changes of atmospheric parameters like temperature. However, the probability to record NLC in the known absence of PMSE remains 7.8%. Regarding all measurements of NLC, 10.1% of NLC occurred without accompanying PMSE. As most, but not all NLC layers are completely embedded into PMSE layers, the actual percentage of volume of NLC without PMSE is even higher. We have shown that the probability to observe NLC without PMSE is highest for large solar zenith angles, when the electron density is low and therefore conclude that electron density plays the major role in the depletion of PMSE when the presence of ice is confirmed by lidar. Both NLC and PMSE are tracers of ice mass, which is dependent on temperature and water vapour content. As lidar measurements of NLC are restricted to a part of the ice particle population and PMSE is additionally influenced by electron density and turbulent activity, it is useful to combine both observations.

Acknowledgements. We gratefully acknowledge the support of the ALOMAR staff with operation of the instruments. We thank P. Hoffmann for providing wind data from the MF radar at ALOMAR to us. Electron densities from the IRI model were calculated with code available from ftp://nssdcftp.gsfc.nasa.gov/models/ionospheric/iri/iri2007/.
This project received research funding from CAWSES/SOLEIL.

Edited by: W. Ward

References

Backhouse, T. W.: The luminous cirrus cloud of June and July, Meterol. Mag., 20, 133–133, 1885.

Baumgarten, G. and Fiedler, J.: Vertical structure of particle properties and water content in noctilucent clouds, Geophys. Res. Lett., 35, L10811, doi:10.1029/2007GL033084, 2008.

Baumgarten, G., Fiedler, J., Lübken, F.-J., and von Cossart, G.: Particle properties and water content of noctilucent clouds and their interannual variation, J. Geophys. Res., 113, D06203, doi:10.1029/2007JD008884, 2008.

Bilitza, D.: The E- and D-region in IRI, Adv. Space Res, 21, 871–874, doi:10.1016/S0273-1177(97)00645-5, 1998.

Bremer, J., Hoffmann, P., Latteck, R., and Singer, W.: Seasonal and long-term variations of PMSE from VHF radar observations at Andenes, Norway, J. Geophys. Res., 108(D8), 8438, doi:10.1029/2002JD002369, 2003.

Bremer, J., Hoffmann, P., Latteck, R., Singer, W., and Zecha, M.: Long-term changes of (polar) mesosphere summer echoes, J. Atmos. Solar Terr. Phys., 71, 1571–1576, doi:10.1016/j.JASTP.2009.03.010, 2009.

Cho, J. Y. N. and Röttger, J.: An updated review of polar mesosphere summer echoes: Observation, theory, and their relationship to noctilucent clouds and subvisible aerosols, J. Geophys. Res., 102, 2001–2020, doi:10.1029/96JD02030, 1997.

Cho, J. Y. N., Hall, T. M., and Kelley, M. C.: On the role of charged aerosols in polar mesosphere summer echoes, J. Geophys. Res., 97, 875–886, 1992.

Chu, X., Espy, P. J., Nott, G. J., Diettrich, J. C., and Gardner, C. S.: Polar mesospheric clouds observed by an iron Boltzmann lidar at Rothera (67.5° S, 68.0° W), Antarctica from 2002 to 2005: Properties and implications, J. Geophys. Res., 111, D20213, doi:10.1029/2006JD007086, 2006.

David, F. N.: Tables of the Ordinates and Probability Integral of the Distribution of the Correlation Coefficient in Small Samples, Biometrika Office, University College, London, Cambridge University Press, UK, 1938.

Ecklund, W. L. and Balsley, B. B.: Long-term observations of the Arctic mesosphere with the MST radar at Poker Flat, Alaska, J. Geophys. Res., 86, 7775–7780, doi:10.1029/JA086iA09p07775, 1981.

Fiedler, J., Baumgarten, G., and von Cossart, G.: Mean diurnal variations of noctilucent clouds during 7 years of lidar observations at ALOMAR, Ann. Geophys., 23, 1175–1181, doi:10.5194/angeo-23-1175-2005, 2005.

Fiedler, J., Baumgarten, G., and Lübken, F.-J.: NLC observations during one solar cycle above ALOMAR, J. Atmos. Solar Terr. Phys., 71, 424–433, doi:10.1016/j.JASTP.2008.11.010, 2009.

Hansen, G., Serwazi, M., and von Zahn, U.: First detection of a noctilucent cloud by lidar, Geophys. Res. Lett., 16, 1445–1448, doi:10.1029/GL016i012p01445, 1989.

Hervig, M. E., Gordley, L. L., Stevens, M. H., Russell, J. M., Bailey, S. M., and Baumgarten, G.: Interpretation of SOFIE PMC measurements: Cloud identification and derivation of mass density, particle shape, and particle size, J. Atmos. Sol.-Terr. Phys., 71, 316–330, doi:10.1016/j.JASTP.2008.07.009, 2009a.

Hervig, M. E., Stevens, M. H., Gordley, L. L., Deaver, L. E., Russell, J. M., and Bailey, S. M.: Relationships between polar mesospheric clouds, temperature, and water vapor from Solar Occultation for Ice Experiment (SOFIE) observations, J. Geophys. Res., 114, D20203, doi:10.1029/2009JD012302, 2009b.

Hervig, M. E., Rapp, M., Latteck, R., and Gordley, L. L.: Observations of mesospheric ice particles from the ALWIN radar and SOFIE, J. Atmos. Sol.-Terr. Phys., doi:10.1016/j.jastp.2010.08.002, in press, 2011.

Hocking, W. K.: Measurement of turbulent energy dissipation rates in the middle atmosphere by radar techniques: A review, Radio Sci., 20, 1403–1422, doi:10.1029/RS020i006p01403, 1985.

Hoffmann, P., Singer, W., and Bremer, J.: Mean seasonal and diurnal variations of PMSE and winds from 4 years of radar observations at ALOMAR, Geophys. Res. Lett., 26, 1525–1528, doi:10.1029/1999GL900279, 1999.

Hoffmann, P., Rapp, M., Serafimovich, A., and Latteck, R.: On the occurrence and formation of multiple layers of polar mesosphere summer echoes, Geophys. Res. Lett., 32, L05812, doi:10.1029/2004GL021409, 2005.

Hoffmann, P., Rapp, M., Fiedler, J., and Latteck, R.: Influence of tides and gravity waves on layering processes in the polar summer mesopause region, Ann. Geophys., 26, 4013–4022, doi:10.5194/angeo-26-4013-2008, 2008.

Jesse, O.: Auffallende Abenderscheinungen am Himmel, Meteorol. Z., 2, 311–312, 1885.

Kelley, M. C., Farley, D. T., and Roettger, J.: The effect of cluster ions on anomalous VHF backscatter from the summer polar mesosphere, Geophys. Res. Lett., 14, 1031–1034, doi:10.1029/GL014i010p01031, 1987.

Kirkwood, S., Cho, J., Hall, C. M., Hoppe, U., Murtagh, D. P., Stegman, J., Swartz, W. E., van Eyken, A. P., Wannberg, G., and Witt, G.: A comparison of PMSE and other ground-based observations during the NLC-91 campaign, J. Atmos. Sol.-Terr. Phys., 57, 35–44, 1995.

Klekociuk, A. R., Morris, R. J., and Innis, J. L.: First Southern Hemisphere common-volume measurements of PMC and PMSE, Geophys. Res. Lett., 35, L24804, doi:10.1029/2008GL035988, 2008.

Klostermeyer, J.: On the diurnal variation of polar mesosphere summer echoes, Geophys. Res. Lett., 26, 3301–3304, doi:10.1029/1999GL003629, 1999.

Latteck, R., Singer, W., and Bardey, H.: The ALWIN MST radar: Technical design and performance, in: European Rocket and Balloon Programs and Related Research, edited by: Schürmann, B., European Space Agency, ESA-SP, 437, p. 179, 1999.

Latteck, R., Singer, W., Morris, R.J., Holdsworth, D.A. and Murphy, D.J.: Observation of polar mesosphere summer echoes with calibrated VHF radars at (69° N) in the Northern and Southern Hemispheres, Geophys. Res. Lett., 34, L14805, doi:10.1029/2007GL030032, 2007.

Leslie, R. C.: Sky glows, Nature, 30, 512–51, doi:10.1038/030512b0, 1885.

Li, Q., Rapp, M., Röttger, J., Latteck, R., Zecha, M., Strelnikova, I., Baumgarten, G., Hervig, M., Hall, C., and Tsutsumi, M.: Microphysical parameters of mesospheric ice clouds derived from calibrated observations of polar mesosphere summer echoes at Bragg wavelengths of 2.8 m and 30 cm, J. Geophys. Res., 115, D00I13, doi:10.1029/2009JD012271, 2010.

Lübken, F.-J. and Höffner, J.: Experimental evidence for ice particle interaction with metal atoms at the high latitude summer mesopause region, Geophys. Res. Lett., 331, L08103, doi:10.1029/2004GL019586, 2004.

Lübken, F.-J., Zecha, M., Höffner, J., and Röttger, J.: Temperatures, polar mesosphere summer echoes, and noctilucent clouds over Spitsbergen (78° N), J. Geophys. Res., 109, D11203, doi:10.1029/2003JD004247, 2004.

Lübken, F.-J., Baumgarten, G., Fiedler, J., Gerding, M., Höffner, J., and Berger, U.: Seasonal and latitudinal variation of noctilucent cloud altitudes, Geophys. Res. Lett., 35, L06801, doi:10.1029/2007GL032281, 2008.

Lübken, F.-J., Lautenbach, J., Höffner, J., Rapp, M., and Zecha, M.: First continuous temperature measurements within polar mesosphere summer echoes, J. Atmos. Sol.-Terr. Phys., 71, 453–463, doi:10.1016/j.JASTP.2008.06.001, 2009.

Lübken, F.-J.: Thermal structure of the arctic summer mesosphere, J. Geophys. Res., 104, 9135–9149, doi:10.1029/1999JD900076, 1999.

Nussbaumer, V., Fricke, K. H., Langer, M., Singer, W., and von Zahn, U.: First simultaneous and common volume observations of noctilucent clouds and polar mesosphere summer echoes by lidar and radar, J. Geophys. Res., 101, 19161–19168, doi:10.1029/96JD01213, 1996.

Rapp, M. and Lübken, F.-J.: On the nature of PMSE: Electron diffusion in the vicinity of charged particles revisited, J. Geophys. Res., 108(D8), 8437, doi:10.1029/2002JD002857, 2003.

Rapp, M. and Lübken, F.-J.: Polar mesosphere summer echoes (PMSE): Review of observations and current understanding, Atmos. Chem. Phys., 4, 2601–2633, doi:10.5194/acp-4-2601-2004, 2004.

Rapp, M., Gumbel, J., Lübken, F.-J., and Latteck, R.: D region electron number density limits for the existence of polar mesosphere summer echoes, J. Geophys. Res., 107(D14), 4187, doi:10.1029/2001JD001323, 2002.

Rapp, M., Strelnikova, I., Latteck, R., Hoffmann, P., Hoppe, U.-P., Häggström, I., and Rietveld, M.: Polar Mesosphere Summer Echoes (PMSE) studied at Bragg wavelengths of 2.8 m, 67 cm, and 16 cm, J. Atmos. Sol.-Terr. Phys., 70, 947–961, doi:10.1016/j.JASTP.2007.11.005, 2008.

Rapp, M., Strelnikova, I., Strelnikov, B., Latteck, R., Baumgarten, G., Li, Q., Megner, L., Gumbel, J., Friedrich, M., Hoppe, U.-P., and Robertson, S.: First in situ measurement of the vertical distribution of ice volume in a mesospheric ice cloud during the ECOMA/MASS rocket-campaign, Ann. Geophys., 27, 755–766, doi:10.5194/angeo-27-755-2009, 2009.

Singer, W., Latteck, R., Hoffman, P., Williams, B. P., Fritts, D. C., Murayama, Y., and Sakanoi, K.: Tides near the Arctic summer mesopause during the MaCWAVE/MIDAS summer program, Geophys. Res. Lett., 32, L07S90, doi:10.1029/2004GL021607, 2005.

Swarnalingam, N., Hocking, W. K., Singer, W., and Latteck, R.: Calibrated measurements of PMSE strengths at three different locations observed with SKiYMET radars and narrow beam VHF radars, J. Atmos. Sol.-Terr. Phys., 71, 1807–1813, doi:10.1016/j.JASTP.2009.06.014, 2009.

Taylor, M. J., van Eyken, A. P., Rishbeth, H., Witt, G., and Witt, N.: Simultaneous observations of noctilucent clouds and polar mesospheric radar echoes – Evidence of non-correlation, Planet. Space Sci., 37, 1013–1017, doi:10.1016/0032-0633(89)90056-1, 1989.

Taylor, M. J., Zhao, Y., Pautet, P., Nicolls, M. J., Collins, R. L., Barker-Tvedtnes, J., Burton, C. D., Thurairajah, B., Reimuller, J., Varney, R. H., Heinselman, C. J., and Mizutani, K.: Coordinated optical and radar image measurements of noctilucent clouds and polar mesospheric summer echoes, J. Atmos. Sol.-Terr. Phys., 71, 675–687, doi:10.1016/j.JASTP.2008.12.005, 2009.

von Cossart, G., Fiedler, J., and von Zahn, U.: Size distributions of NLC particles as determined from 3-color observations of NLC by ground-based lidar, Geophys. Res. Lett., 26, 1513–1516, doi:10.1029/1999GL900226, 1999.

von Zahn, U. and Bremer, J.: Simultaneous and common-volume observations of noctilucent clouds and polar mesosphere summer echoes, Geophys. Res. Lett., 26, 1521–1524, doi:10.1029/1999GL900206, 1999.

von Zahn, U., von Cossart, G., Fiedler, J., Fricke, K. H., Nelke, G., Baumgarten, G., Rees, D., Hauchecorne, A., and Adolfsen, K.: The ALOMAR Rayleigh/Mie/Raman lidar: objectives, configuration, and performance, Ann. Geophys., 18, 815–833, doi:10.1007/s00585-000-0815-2, 2000.